Bioactive Materials 37 (2024) 393–406

Contents lists available at ScienceDirect

Bioactive Materials

journal homepage: www.keaipublishing.com/en/journals/bioactive-materials

Biosynthesis of fungus-based oral selenium microcarriers for radioprotection and immuno-homeostasis shaping against radiation-induced heart disease

Chang Liu [a,b,1], Weiyi Wang [c,1], Haoqiang Lai [c], Yikang Chen [d], Lvyi Li [c], Haiwei Li [d], Meixiao Zhan [a], Tianfeng Chen [a,c,*], Wenqiang Cao [b,**], Xiaoling Li [c,***]

[a] Zhuhai People's Hospital (Zhuhai Clinical Medical College of Jinan University), Zhuhai, 519000, PR China
[b] Zhuhai Jinan Selenium Source Nanotechnology Co., Ltd, Jinan University, Zhuhai 519000, China
[c] Department of Chemistry, Institute of Food Safety and Nutrition, Jinan University, Guangzhou 510632, China
[d] Guangdong Jinan Established Selenium Source Nano Technology Research Institute Co., Ltd., Guangzhou 510535, China

ARTICLE INFO

Keywords:
Radiation-induced heart disease
Antioxidant
Selenium
Selenoprotein
Heart protection

ABSTRACT

Radiation-induced heart disease (RIHD), characterized by severe oxidative stress and immune dysregulation, is a serious condition affecting cancer patients undergoing thoracic radiation. Unfortunately, clinical interventions for RIHD are lacking. Selenium (Se) is a trace element with excellent antioxidant and immune-modulatory properties. However, its application in heart radioprotection remains challenging. Herein, we developed a novel bioactive *Cordyceps militaris*-based Se oral delivery system (Se@*CM*), which demonstrated superior radioprotection effects *in vitro* against X-ray-induced damage in H9C2 cells through suppressing excessive ROS generation, compared to the radioprotectant Amifostine. Moreover, Se@*CM* exhibited exceptional cardioprotective effects *in vivo* against X-ray irradiation, reducing cardiac dysfunction and myocardial fibrosis by balancing the redox equilibrium and modulating the expression of Mn-SOD and MDA. Additionally, Se@*CM* maintained immuno-homeostasis, as evidenced by the upregulated population of T cells and M2 macrophages through modulation of selenoprotein expression after irradiation. Together, these results highlight the remarkable antioxidant and immunity modulation properties of Se@*CM* and shed light on its promising application for cardiac protection against IR-induced disease. This research provides valuable insights into developing effective strategies for preventing and managing RIHD.

1. Introduction

Despite substantial advancements in radiation therapy technology, patients undergoing radiation therapy still suffer varying degrees of non-specific radiation damage to healthy tissues, causing significant distress [1]. During the radiotherapy treatment of thoracic tumors such as those located in the mediastinum, lower end of the esophagus and left breast, even with advanced radiotherapy techniques, the heart will inevitably receive some radiation, leading to radiation-induced heart disease (RIHD) [2,3]. When exposed to radiation, the myocardium generates a large amount of ROS due to radiation ionization in water. Oxidative stress occurs when the body's natural oxidative capacity is inadequate to remove excessive ROS, which can result in RIHD [4,5]. Various pharmacological agents, such as Amifostine (AMI), angiotensin-converting enzyme inhibitors and statins, have shown promise in preclinical and early clinical studies for their potential to protect the heart from irradiation injury. Furthermore, with the rapid development of nanomaterials, their application in nano-radiation protection therapy has been widely investigated, benefiting from their high efficiency, low toxicity, and prolonged circulation characteristics [3,6]. Among them,

Peer review under responsibility of KeAi Communications Co., Ltd.
* Corresponding author. Zhuhai People's Hospital (Zhuhai Clinical Medical College of Jinan University), Zhuhai, 519000, PR China.
** Corresponding author.
*** Corresponding author.
E-mail addresses: tchentf@jnu.edu.cn (T. Chen), sesource_cwq@163.com (W. Cao), tlxlli@jnu.edu.cn (X. Li).
[1] These authors contributed equally to this work.

https://doi.org/10.1016/j.bioactmat.2024.03.034
Received 23 December 2023; Received in revised form 28 March 2024; Accepted 29 March 2024

nanoenzymes with strong antioxidant effects are most commonly used in radiation protection therapy, and significant protective effects have also been achieved at the cellular and animal levels, such as nanoenzymes based on cerium oxide [7,8] and carbon nanoparticles [9]. Although nanotechnology has made many promising advances in the application of radiation-protective drugs, there is still a significant gap to overcome for large-scale practical application. Besides, with the widespread use of traditional Chinese medicine, it has been proven that Danshen, Danggui, Huangqi, and other herbs can alleviate radiation-induced cardiac fibrosis [10]. So far, the pathological mechanisms of RIHD remain unresolved, and there are no effective drugs available. Therefore, effective strategies to inhibit RIHD will be of great clinical significance.

Selenium (Se) is a trace element for human health, playing a vital role in preventing illness and disease. By incorporating into selenoproteins, Se exerts diverse pleiotropic effects, including antioxidant, anti-inflammatory, anti-tumor, and immunomodulatory [11–13]. In our previous studies, the administration of selenium nanoparticles (SeNPs) and Se-containing complex have been shown to enhance the cytotoxicity of NK cells and γδT cells [14–17]. Moreover, SeNPs were found to restore the dysfunctional immune cells in the patient-derived MPE microenvironment [18]. Furthermore, Se supplementation has demonstrated remarkable anti-inflammatory effects by reprogramming the immune microenvironment at sites of inflammation [19,20]. SeNPs have also shown sound protective effects against cisplatin-induced nephrotoxicity and palmitic acid-induced pancreatic β damage by eliminating ROS and maintaining oxidative balance in cellular [21,22]. Moreover, the U.S. National Academy of Sciences approved Se as a dietary antioxidant that noticeably decreases the side effects of reactive species [23]. For instance, in a mouse model of oral mucositis induced by X-ray irradiation, sodium selenite demonstrated a protective effect against irradiation [24]. These findings highlight the potential for developing novel Se-based agents as radioprotectants to combat radiation-induced heart disease (RIHD) and maintain immune system homeostasis.

Nowadays, oral administration remains the preferred drug delivery system due to its myriad advantages. To surmount biological barriers, there has been a growing interest in developing biomimetic and bio-inspired strategies [25,26]. Plant-based drug delivery platforms have shown great promise in enhancing bioavailability, drug distribution and therapeutic efficacy [27,28]. Moreover, these systems provide a renewable and sustainable approach that is biocompatible, non-toxic and minimizes the risk of adverse reactions. One such plant-based system is *Cordyceps militaris* (*CM*), an ethnomedicinal fungus with significant importance in traditional Chinese medicines. *CM* is widely used as both a crude drug and functional food in Asia [29]. It exhibits a diverse biological activities, including anti-bacterial [30], anti-inflammatory [31], anti-aging [32], anti-oxidation [33,34], anti-tumor [35] and immunomodulatory effects [33]. Notably, cordycepin, a major active ingredient of *CM*, was reported to prevent radiation ulcers by inhibiting cell senescence [36]. Therefore, developing a *CM*-based agent is reasonable to prevent and treat oxidative disorder diseases effectively.

Herein, *CM* was used as a versatile carrier for SeNPs to develop an oral drug delivery system (Se@*CM*) for the treatment of RIHD (Fig. 1A). Se@*CM* protected normal heart tissue against X-ray irradiation by eliminating the overproduction of ROS, and thus reducied ROS-induced DNA damage and ER stress. In addition, we also found that Se@*CM* exhibited a regulation role in maintaining the homeostasis of immunity *in vivo* through modulating the proportion of T cells and M2 macrophages. In all, this study presents a promising strategy for protecting the heart from X-ray-induced damage.

2. Results

2.1. Characterization of Se@CM

Se@*CM* was obtained by adding Selenium nanoparticles (SeNPs) in the culture medium of *CM* in this study. The particle size and Zeta potential of SeNPs was about 60 nm and −12 mV, respectively (Fig. S1). Although 60 μg/g of SeNPs were added in the cultural medium, the growth yield of Se@*CM* was not affected as shown in Fig. 1B, which indicated the safety of SeNPs for *Cordyceps militaris*. Then, the Se content in *CM* and Se@*CM* was detected by the Atomic Fluorescence Spectrometer (AFS) method. As shown in Fig. 1C, the content of Se in *CM* is only 1.58 ± 0.38 μg/g. While, the selenium content in Se@*CM* is substantially higher, reaching up to 120.9 ± 17.92 μg/g. However, in terms of other active substances such as cordycepin and cordycepic acid, there were no notable variations between *CM* and Se@*CM* (Fig. 1D), and essential amino acid (Fig. 1E). UV–vis was employed to detect the absorption wavelength of *CM* and Se@*CM*, and there was an obvious absorption peak of Se@*CM* in 400–500 nm, while the peak of *CM* was not obvious (Fig. 1F). Besides, we also detected the absorption of Se@*CM* at different concentrations. As shown in Fig. 1G, the absorption peak in 400–500 nm of Se@*CM* had obvious concentration dependence. Together, these results demonstrate that except for the content of Se, there were no significant differences between *CM* and Se@*CM*.

2.2. Se@CM restrained X-ray-induced cell proliferation suppression in H9C2 cells

To evaluate the biomedical applications of Se@*CM* on H9C2 cells, the cytotoxic effect was evaluated using a 3-(4,5)-dimethylthiahiazo (-z-y1)-3,5-di- phenytetrazoliumromide (MTT) assay. No significant cytotoxicity effects were observed with Se@*CM* treatment across a concentration ranging from 0.19 to 12.5 μg/mL. While, 3.1 μg/mL of *CM* exhibited obvious growth suppression effects, suggesting that Se introduction may enhance the biosafety of *CM* (Fig. 2A). Interestingly, *CM* loaded with Se was also observed to facilitate the proliferation of H9C2 cells, which may indicate the specific roles of Se in regulating cell growth. To assess the protective effects of Se@*CM* against X-ray irradiation, an MTT assay was employed. After radiation exposure, the viability of H9C2 cells decreased to 86.0%, 78.7% and 67.8% at doses of 4 Gy, 8 Gy and 16 Gy, respectively, as shown in Fig. 2B. However, Se@*CM* pretreatment of H9C2 cells dramatically restrained the growth suppression effects induced by 16 Gy X-ray irradiation at the concentration range of 0.19–6.25 μg/mL, which exhibited better protection properties than *CM* alone treatment (Fig. 2C). The morphologies changes of H9C2 cells also confirmed the protective effect of Se@*CM* and *CM* against X-ray irradiation (Fig. S2). Additionally, we also conducted Calcein-AM/PI double staining assay and colony formation assays to evaluate the radioprotection properties of Se@*CM*. As shown in Fig. 2D, X-ray (16 Gy) could induce cell death in time dependence, and the radioprotectant AMI treatment was found to restrain this damaging effect. However, 5 μg/mL of Se@*CM* preincubation exhibited better protective effects against X-ray (16 Gy) when compared with *CM* or AMI treatment under different incubation times as indicated by the decreased red fluorescence intensity. Furthermore, better protective effects can be observed in H9C2 cells upon the incubation of 5 μg/mL of Se@*CM* under 16 Gy irradiation when compared with *CM* or AMI treatments. Moreover, Adenosine Triphosphate (ATP) is the most direct source of energy in organisms and is widely used in muscle contraction, metabolic reaction, and active transportation. The ATP content was significantly decreased after X-ray irradiation; however, the pretreatment of Se@*CM*, *CM* and AMI could inhibit the decrease of ATP, especially for Se@*CM* (Fig. S3). As illustrated in Fig. 2E&F, the formations of cell colonies were significantly inhibited by X-ray irradiation; the survival fractions were decreased to 0.74 ± 0.04, 0.64 ± 0.04, and 0.39 ± 0.02 for 4 Gy, 8 Gy and 16 Gy irradiation, respectively, while 1.28 ± 0.03 and 1.13 ± 0.08 were achieved by the 24 h preexposure of *CM* (5 μg/mL) and AMI (2 μM) (folds of Control), respectively. By contrast, Se@*CM* significantly improved the cell colony formation of irradiated cells with enhanced folds at 1.51 ± 0.084 when comparing with the control group. Besides, compared with X-ray irradiation alone, pre-treatment with Se@*CM*, *CM*,

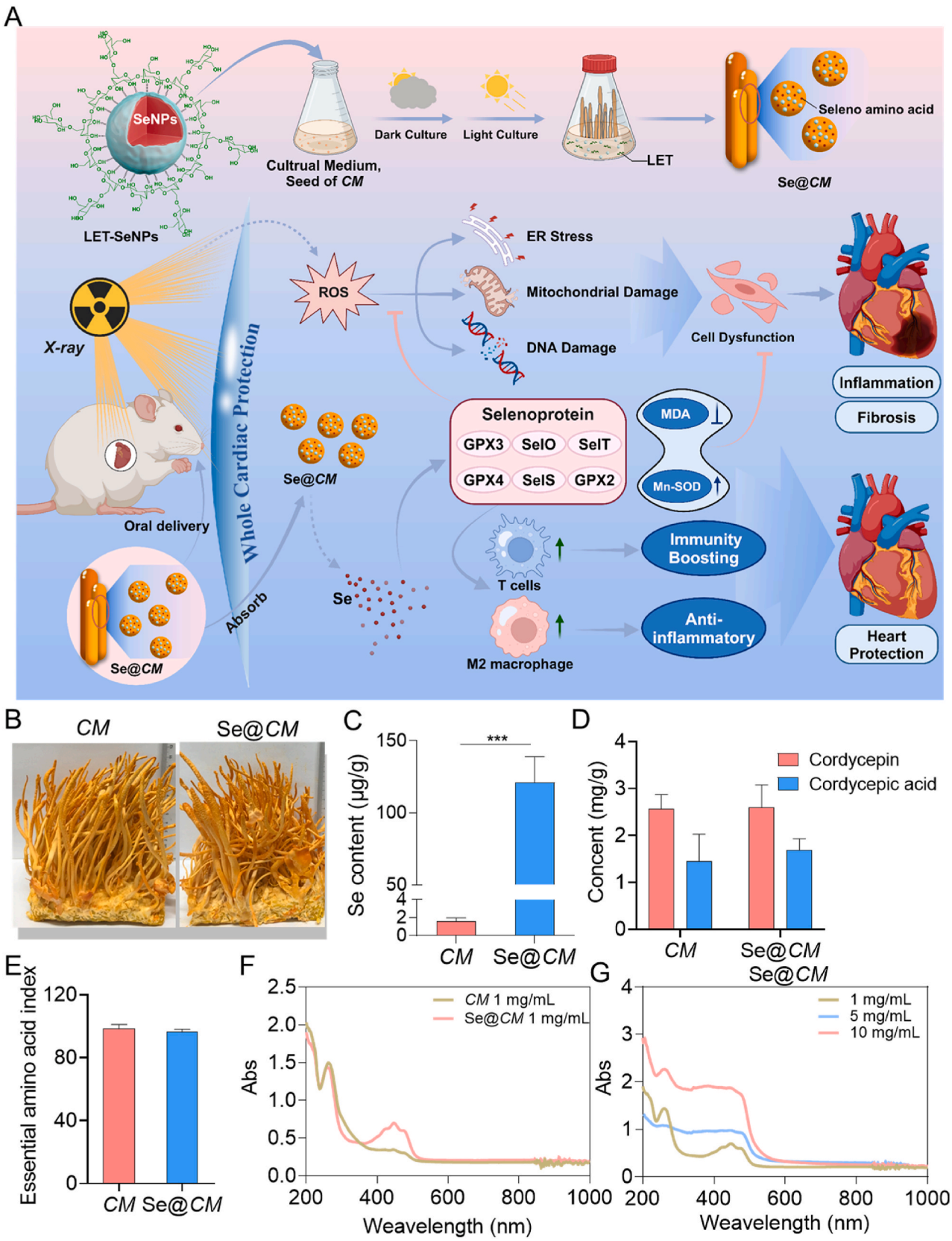

Fig. 1. Design and characterization of the Se@*CM*. (A) Schematic illustration of synthetic protocols and the role of Se@*CM* on cardiomyocytes against X-ray irradiation. (B) Images of *CM* and Se@*CM*. (C) The content of Se in *CM* and Se@*CM*. (D) The cordycepin and cordycepic acid of *CM* and Se@*CM*. (E) The essential amino acid index of *CM* and Se@*CM*. (F) The UV absorption spectroscopy of 1 mg/mL of *CM* and Se@*CM*. (G) The UV absorption spectroscopy of different concentrations of Se@*CM*. Each value represents as mean ± SD of triplicates, n = 3, ***$P < 0.001$.

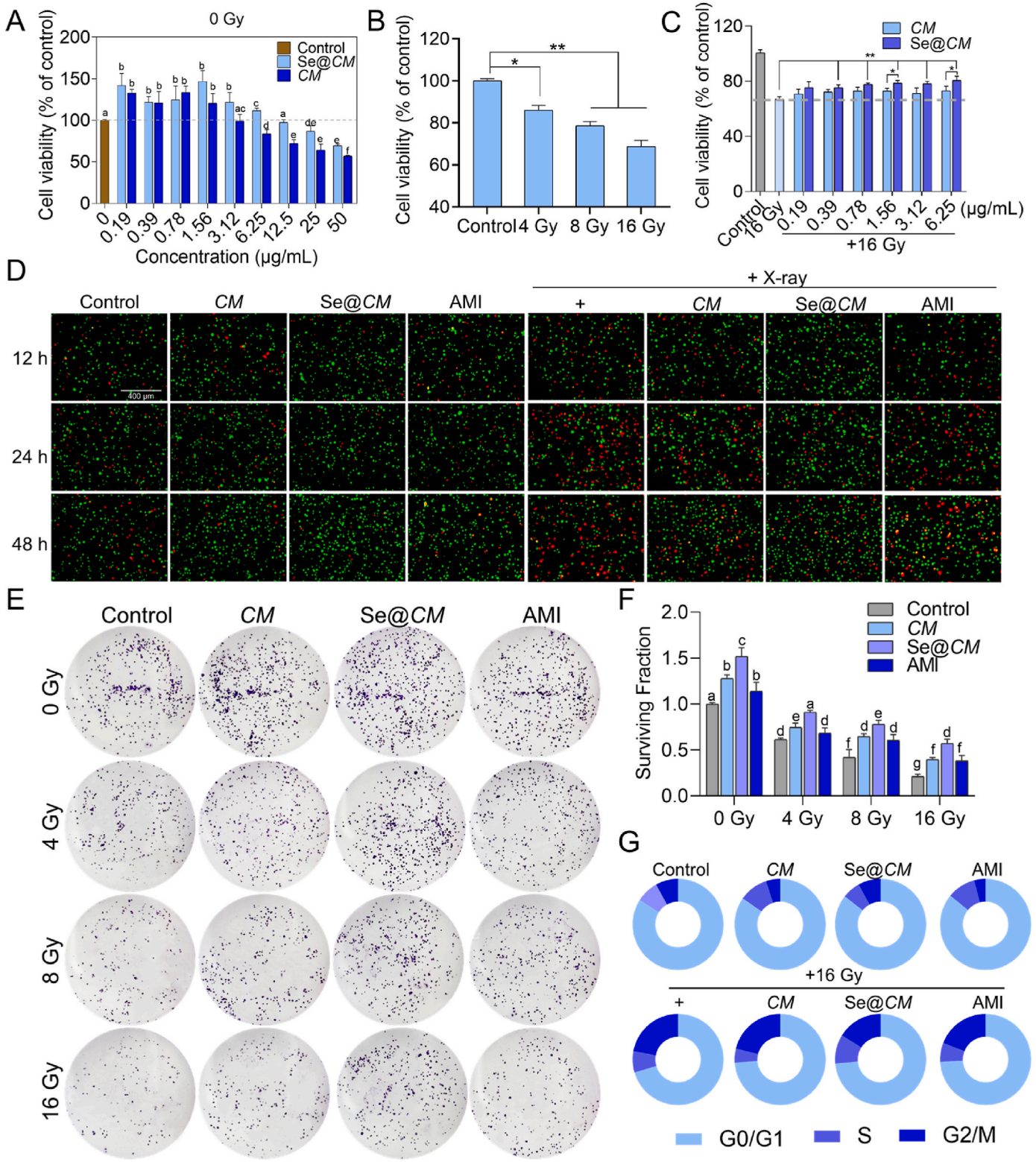

Fig. 2. Protection effects of Se@*CM* on H9C2 cells against X-ray. (A) Cytotoxic effect of different concentrations (0.19–50 μg/mL) of Se@*CM* and *CM* on H9C2 cells for 72 h. (B) Cell viability of H9C2 cells exposed to different doses of X-ray. (C) Protection effect of different concentrations (0.19–6.25 μg/mL) of Se@*CM* and *CM* on H9C2 cells against different doses of X-ray (16 Gy). (D) Calcein-AM/PI fluorescence images of H9C2 cells pre-treated with Se@*CM*, *CM* (5 μg/mL), and AMI (2 μM) for 24 h and then irradiated by X-ray (16 Gy) or not (Scale bar = 400 μm). (E) The surviving colonies of H9C2 cells were irradiated by 0, 4, 8, and 16 Gy in different treatment groups (Control, X-ray, *CM*, Se@*CM* and AMI) by crystal violet staining and the quantification analysis (F). H9C2 cells were pre-treated with Se@*CM*, *CM* (5 μg/mL), and AMI (2 μM) for 24 h, and then irradiated by X-ray (16 Gy). (G) Flow cytometric analysis of cell cycle distribution in H9C2 cells after pre-treating with Se@*CM*/*CM* (5 μg/mL), and AMI (2 μM) for 24 h and then treated with X-ray (16 Gy). Each value represents as mean + SD of triplicates, n = 3, $^{*}P < 0.05$, $^{**}P < 0.01$. Characters a - g are statistically different at the $P < 0.05$ level.

and AMI significantly enhanced the formation of cell colonies against X-ray irradiation, whether under doses of 4 Gy, 8 Gy, or 16 Gy (Fig. 2E&F). Among them, Se@*CM* showed the best protective effect on cell cloning. For example, the surviving fraction decreased to 0.21 ± 0.02 fold of control after 16 Gy irradiation. However, the surviving fraction increased to 0.57 ± 0.04 after the pretreatment with Se@*CM*. To investigate whether Se@*CM* also has protective effects on other cells, normal hepatocyte cell line LO2 and regular lung cell line WI38 were selected. As shown in Fig. S4, X-ray (16 Gy) irradiation could significantly inhibit the growth of LO2 cells and WI38 cells, with cell viability at 69.7 ± 4.3% and 54.3 ± 1.6%, respectively. Besides, Se@*CM* and *CM* had no cytotoxicity on these two types of cell lines. Interestingly, Se@*CM* and *CM* showed excellent protective effects against X-ray irradiation, especially Se@*CM*.

We also examined whether the radioprotective properties of Se@*CM* could affect the therapeutic efficacy of radiation therapy for cancer. As shown in Fig. S5, X-ray radiation (16 Gy) had cytotoxicity on these three types of cells, with cell viability of 64.23 ± 8.03% to MDA-MB-231 cells, 73.02 ± 4.34% to MCF-7 cells, and 73.53 ± 7.58% to A549 cells, respectively. Moreover, the cell viability of Se@*CM* + X-ray and *CM* + X-ray was less than X-ray alone in these three types of cells, especially in A549 cells, the cell viability decreased to 52.94 ± 8.62% of Se@*CM* + X-ray. The results suggested that using Se@*CM* did not negatively impact the effectiveness of radiotherapy for treating tumors.

Together, these results suggest that loading Se into the *CM* carrier can enhance its radioprotective effects without compromising the cytotoxicity of radiotherapy on tumor cells.

Cell cycle arrest is one of the major action modes by which X-ray irradiation hinders cell growth and triggers cell death [37]. Hence, we investigated the protective effects of Se@*CM* against radiation-induced alterations in the cell cycle distribution of H9C2 cells using a flow cytometry assay. There were no significant differences in the distribution of cell cycle among the treatment groups with 5 μg/mL of *CM*/Se@*CM* and 2 μM of AMI alone, as illustrated in Fig. 2G and Fig. S6. However, 16 Gy radiation induced a noticeable G2/M phase arrest with cell proportion increased from 6.31% to 22.05% when compared with the control group. The pre-treatment of *CM* showed mild decreasing changes of the G2/M cell population under the exposure of X-ray, which was similar to the radioprotectant AMI treatment with arrested cells population dropped to 21.46% and 19.09%, respectively. Se@*CM* pre-treatment effectively reduced the G2/M cell population to 16.46% after X-ray exposure. In addition, no significant differences were found in the population of Sub-G1 cells among these groups (Fig. S6). Together, these results demonstrated that Se@*CM* displayed excellent radioprotective effects.

2.3. Protective effects against radiation elicit oxidative stress-mediated damages

Mitochondria are vital organelles responsible for generating energy for cell survival. Decreased mitochondrial membrane potential ($\Delta\Psi_m$) is a well-documented indicator of mitochondrial damage. Mitochondrial dysfunction has been strongly associated with radiation-induced damage [38]. Therefore, to evaluate whether Se@*CM* could maintain the homeostasis of mitochondria, a JC-1 probe was used to examine the changes in mitochondria potential in H9C2 cells following X-ray radiation. As depicted in Fig. 3A, the mitochondria membrane potential of H9C2 cells was barely changed after cells were treated with *CM*, Se@*CM* (5 μg/mL) and AMI (2 μM). However, the proportion of mitochondria monomer increased from 4.08% to 39.2% after X-ray irradiation, indicating that mitochondrial damage has occurred. Preincubation with *CM* was found to mitigate radiation damages, similar to AMI treatments with reduced monomer proportion of 29.7% and 29.8%, respectively. However, Se@*CM* pre-treatment triggered a significant downtrend with 24.9% of depolarized mitochondria after X-ray exposure, indicating its protective effects on fully functional mitochondria in H9C2 cells. These results were further confirmed by the changes in fluorescence intensity of JC-1 in aggregate and monomer mitochondria (Fig. 3B & Fig. S7). Indeed, the loss of mitochondrial membrane potential is known to compromise mitochondrial function, potentially leading to the release of cytochrome C and initiation of cell apoptosis. However, radiotherapy can induce stress responses in cells that protect them against apoptosis. This is achieved by upregulating anti-apoptotic proteins such as BCL-2, BCL-XL, and others. Besides, we also studied the changes in PARP, an apoptosis protein, and found that its expression did not change (Fig. S8). These results demonstrated that Se@*CM* was able to effectively reverse mitochondria malfunction triggered by X-ray radiation.

Excessive ROS production has been confirmed to be the main cause of X-ray-induced heart disease. Se@*CM* was found to possess superior free radical scavenging effects against both 2, 2′-azino-bis(3-ethylbenzothiazoline-6-sulfonic acid) (ABTS•) and 1,1-Diphenyl-2-picrylhydrazyl radical 2,2-Diphenyl-1-(2,4,6-trinitrophenyl) hydrazyl (DPPH•) *in vitro* in a time-dependent manner in comparison with *CM* alone treatment (Fig. 3C&D). Furthermore, Se@*CM* exhibited better intracellular ROS generation suppression potency against X-ray irradiation than *CM* and AMI treatment, which indicated the excellent antioxidant activities of Se@*CM* (Fig. 3E). The fluorescence changes of 2′,7′-Dichlorofluorescein (DCF) by fluorescence microscope assay (Fig. 3F) and flow cytometry assay (Fig. S9) upon irradiation in cells pretreated with *CM*, AMI and Se@*CM* also demonstrated the preferable ROS eliminating potency of Se@*CM*. Besides, *Si*-DMA, a fluorescent probe for detecting mitochondrial singlet oxygen, was used for detecting mitochondrial ROS by flow cytometry. As shown in Fig. S10, X-ray irradiation (16 Gy) induced a notable increase in mitochondrial ROS. However, the pre-treatment with Se@*CM* and *CM* could inhibit the generation of mitochondrial ROS significantly, especially for Se@*CM*. In addition, we also validated the protective effect of Se@*CM* in WI38 cells by detecting the changes in mitochondrial membrane potential and ROS induced by X-ray irradiation. The proportion of mitochondria monomer increased from 0.68% to 18.33% after X-ray irradiation, as illustrated in Fig. S11A. However, the pre-treatment of Se@*CM* triggered a significant downtrend with 6.58% of depolarized mitochondria after X-ray exposure, indicating the protective effects on fully functional mitochondria in WI38 cells. The fluorescence changes of DCF by flow cytometry assay also indicated that Se@*CM* could significantly inhibit the generation of ROS induced by X-ray irradiation (Fig. S11B&C).

The total cellular thiols were subsequently studied, as the oxidation-reduction state of cellular thiols is a pivotal in antioxidant defense mechanisms. X-ray irradiation caused a significant decrease in intracellular thiols (Fig. S12), and pre-treatment of Se@*CM* could inhibit the decrease significantly. To further determine the reduction ability of Se@*CM*, an intracellular glutathione (GSH), and Glutathione oxidized (GSSG) assay kit was employed to determine the redox state of H9C2 cells. As shown in Fig. S13, the GSH/GSSG ratio in H9C2 cells was significantly decreased after irradiation by X-ray (16 Gy), which indicates that X-ray irradiation can significantly induce oxidative stress. However, pretreatment with Se@*CM* could significantly prevent the decrease in the GSH/GSSG ratio. Besides, pretreatment with *CM* and AMI also mitigated the decrease in the GSH/GSSG ratio to some extent. These results indicate that Se@*CM* could maintain the intracellular redox balance by preserving the GSH/GSSG ratio.

ROS overproduction has been confirmed to be one of the major action mechanisms in anticancer and inducing healthy tissue injury. Accumulating intracytoplasmic levels of ROS could induce DNA damage, endoplasmic reticulum (ER) stress, and mitochondria dysfunction, ultimately resulting in cellular dysfunction [39]. We observed that exposure to X-ray radiation triggers a DNA damage response, leading to an increase in the expression of proteins such as *p*-ATM, *p*-ATR, *p*-CHK1, *p*-BRCA1 and p-H2A.X (Fig. 3G&Fig. S14). Besides, the DNA damage was also verified by evaluating the expression of p-H2A.X (Ser139) by IF assay in H9C2 cells. As shown in Fig. S15, we found that there is a significant elevation of DNA strand breaks in cells with X-ray irradiation

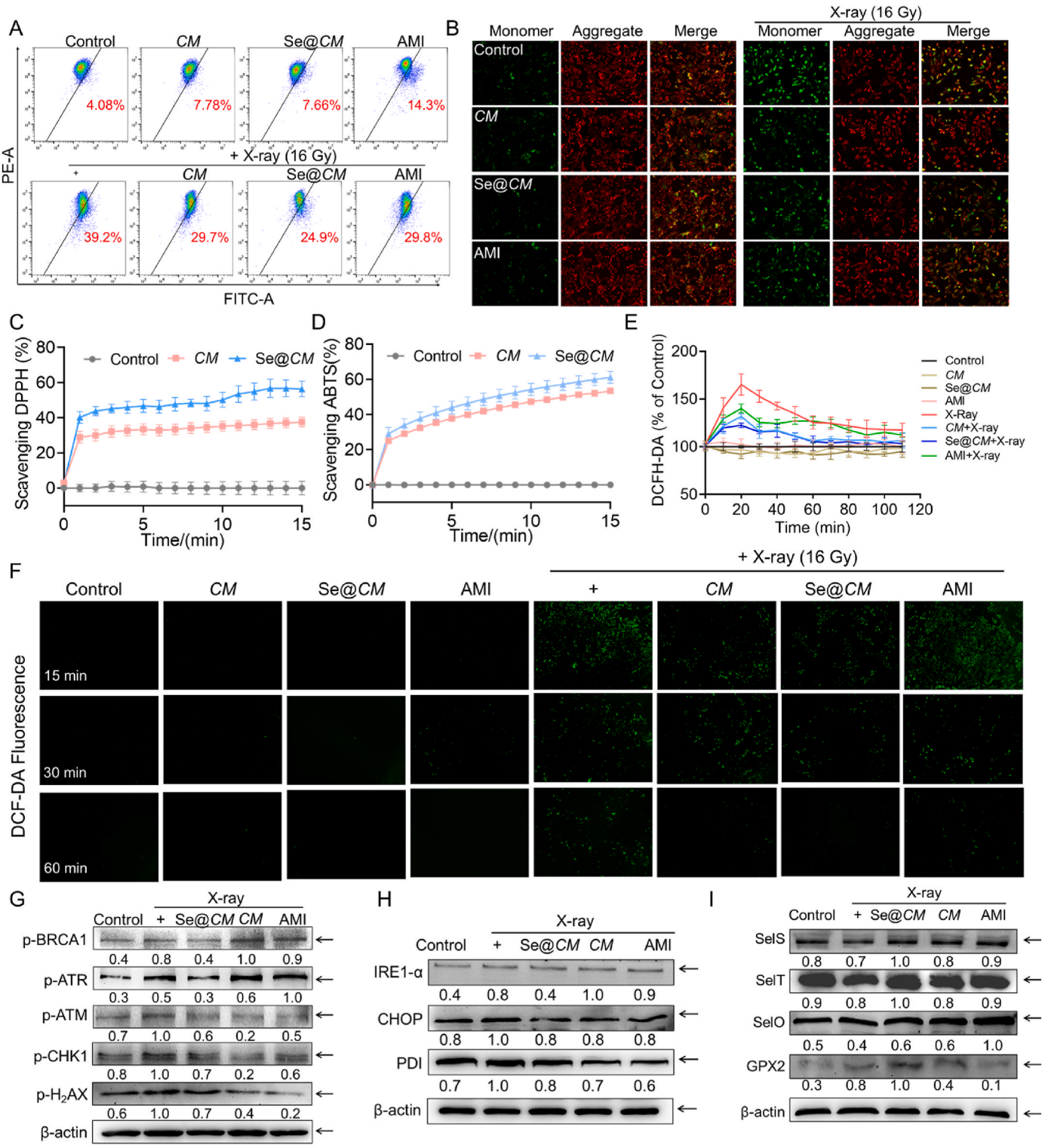

Fig. 3. The protective effect of Se@*CM* on H9C2 cells against X-ray-induced ROS and DNA damage. (A) Changes of $\Delta\Psi$m on H9C2 cells after pre-treated with *CM*/Se@*CM* (5 μg/mL) and AMI (2 μM) for 24 h and then treated with X-ray (16 Gy). (B) Representative fluorescence images of monomer and aggregate mitochondria by staining with JC-1 in H9C2 cells after treating *CM*, Se@*CM*, AMI and X-ray (16 Gy). (C) Absorbance changes along with the time of DPPH· and ABTS· solution (D) after the addition of 10 μg/mL of *CM*/Se@*CM*. (E) Se@*CM* suppressed X-ray induced ROS accumulation in H9C2 cells by staining with DCFH-DA. (F) The representative images of H9C2 cells by staining with DCFH-DA along with time. H9C2 cells were treated with *CM*/Se@*CM* (5 μg/mL) or AMI (2 μM) and then treated with/without X-ray (16 Gy), then the fluorescence values of every group along with time were detected by a fluorescence microplate reader, and the corresponding images were taken at 15 min, 30 min and 1 h, respectively. (G) Protein expression of *p*-BRCA1, *p*-ATM, *p*-ATR, *p*-CHK1 and p-H2A.X. (H) Protein expression of IRE1-α, CHOP, PDI. (I) Protein expression of SelS, SelT, SelO and GPX2. β-actin was used as the internal reference protein. Data are expressed as mean ± SD, n = 3.

(16 Gy). Additionally, the decreased fluorescence intensity indicated significantly inhibited expression of p-H2A.X when pre-treated with Se@*CM*.

Oxidative stress is a major factor that induces ER stress. In our study, ER stress was also found in cells after the radiation of X-ray, evident in increased protein expression levels of CHOP, IRE1-α and PDI (Fig. 3H&Fig. S16). However, Se@*CM* pretreatment potently restrained DNA damage and ER stress, which may be due to the increased redox balancing activities as indicated by the upregulation of antioxidant proteins such as SELS, SELT, SELO and GPX2 (Fig. 3I&Fig. S17). These selenoproteins are involved in promoting inflammation resolution and reducing oxidative stress, both of which are important factors in the development of RIHD. Further investigation is necessary to fully understand the impact of these selenoproteins on RIHD, which could potentially contribute to the progress of targeted therapeutic strategies aimed at reducing or preventing RIHD. In a word, selenoproteins mainly

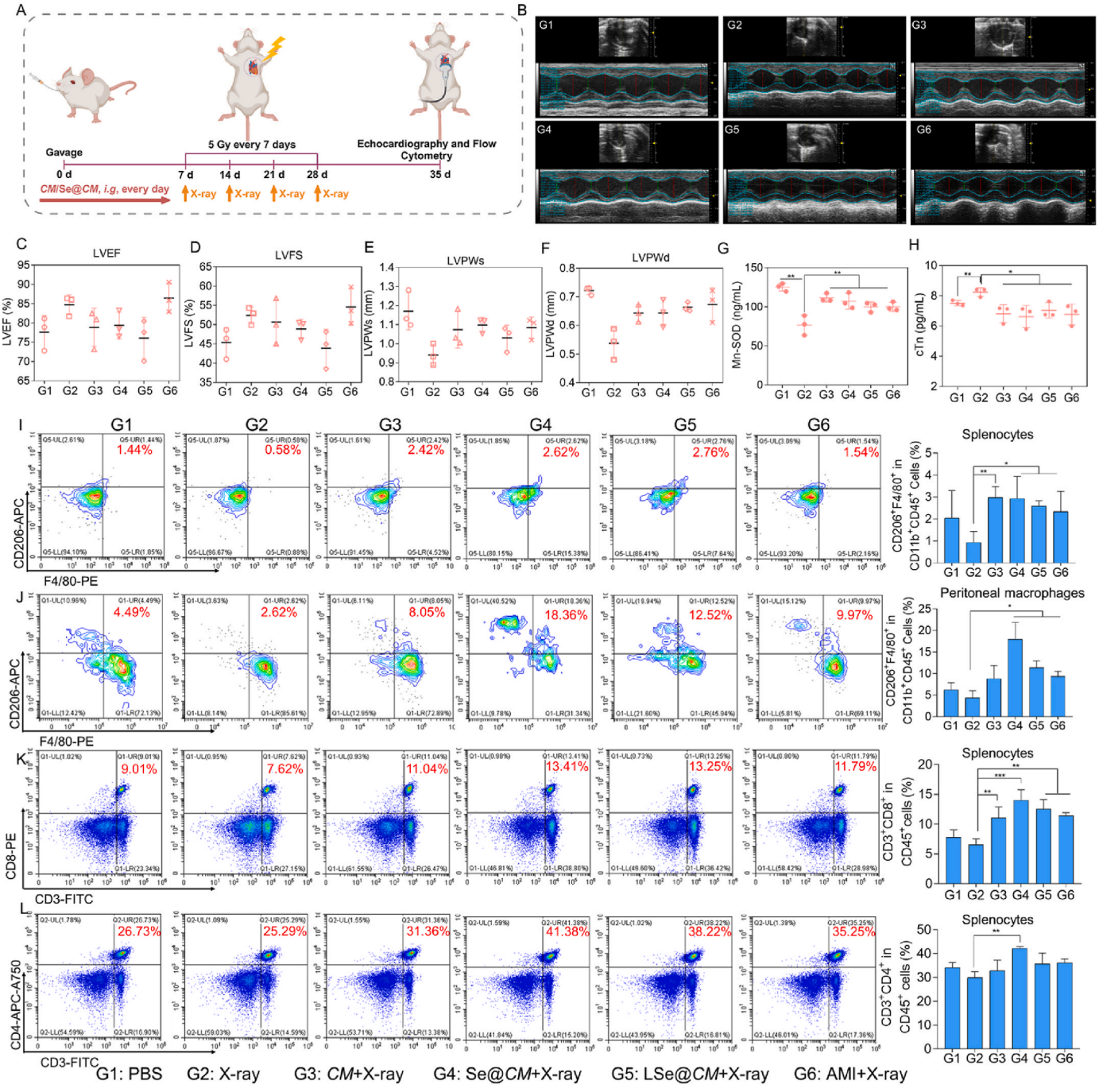

Fig. 4. The protective effect of Se@*CM* on cardiac function against X-ray irradiation *in vivo*. (A) A schematic diagram depicting the treatment of mice with Se@*CM* and X-ray irradiation. (B) Echocardiography detection process and representative M-mode echocardiograms of different treatments after 7 days post the last IR. (C) Left ventricular ejection fraction (LVEF) and (D) left ventricular fraction shortening (LVFS), (E) Left ventricular posterior wall systolic thickness (LVPWs), (F) Left ventricular posterior wall end-diastolic thickness (LVPWd), (G) Manganese-superoxide dismutase (Mn-SOD) and (H) Cardiac troponin (cTn) of different treatments after 7 days post the last IR. (I) The ratio of M2-macrophage ($CD206^+F4/80^+$ in $CD11b^+CD45^+$ cells) in splenocytes, and (J) M2-macrophage in peritoneal macrophages. (K) $CD8^+$ T cells in splenocytes, and (L) $CD4^+$ T cells in splenocytes of different treatments at day 7th post the last IR. Each value represents as mean ± SD, n = 3, $^*P < 0.05$, $^{**}P < 0.01$, $^{***}P < 0.001$.

resist radiation-induced damage by regulating the cellular redox state, thereby inhibiting DNA damage and ER stress induced by X-ray irradiation.

2.4. Biocompatibility, pharmacokinetics and distribution studies

In order to evaluate the biocompatibility of Se@*CM*, the hemocompatibility assay was conducted. As shown in Fig. S18, no apparent hemolysis was observed, and there were no discernible morphological changes in red blood cells following a 2-h incubation with *CM* and Se@*CM*, respectively.

The pharmacokinetics and distribution studies were performed in Balb/c mice. The Se plasma concentration-time curve as shown in Fig. S19A, and the major pharmacokinetic parameters were shown in Fig. S19B. The concentration-time curve of Se was fitted two compartment model. After administration of Se@*CM* by gavage, the content of Se was significantly increased and peaked at about 2.23 h. The $T_{1/2\beta}$ and MRT were 79.08 h and 101.78 h, respectively. Besides, the Se content in major organs, such as the heart, liver, spleen, lung, kidney and intestine was detected as shown in Fig. S20. Se@*CM* was primarily absorbed in the small intestine, reaching its peak concentration within the intestine at 0.5 h post-administration, indicating the rapid absorption. Subsequently, Se@*CM* entered the blood circulation and is distributed to various tissues. Post-administration, the Se levels in the heart gradually rise, peaking at 2–8 h, and then gradually declining. The Se level changes observed in lung tissue mirror those in the heart. Furthermore, Se@*CM* shows significant accumulation in the liver, spleen and kidneys, suggesting potential metabolism in the liver and spleen, with subsequent excretion through the kidneys.

2.5. In vivo protection effect on cardiac function against X-ray-induced damage

Then, we assessed the protective effects of Se@*CM* against X-ray irradiation in mice, and the treatment schedule is shown in Fig. 4A. As shown in Fig. S21, radiotherapy caused obvious body weight loss in mice received with X-ray irradiation. However, mice given Se@*CM* did not show a significant increase in body weight, indicating a potential protection role of Se against X-ray radiation. After 7 days of the last irradiation, three mice from every group were randomly selected for echocardiography (Fig. 4B). Compared to healthy mice, the LVEF (left ventricular ejection fraction) and LVFS (left ventricular shortening fraction) were significantly increased after exposed to X-ray (Fig. 4C&D). However, the treatment of *CM*/Se@*CM* could inhibit the increase of LVEF and LVFS, particularly in the case of LSe@*CM* + X-ray group. Besides, the LVPWs (left ventricular posterior wall systolic thickness) and LVPWd (left ventricular posterior wall end-diastolic thickness) were significantly decreased after 20 Gy irradiation (Fig. 4E&F), while these were not significantly changed in the group of *CM*/Se@*CM* treatment. These results suggest that X-ray irradiation could induce damage to heart function, and the treatment of Se@*CM* could inhibit X-ray-induced damage. Besides, we also examined if X-ray irradiation could induce damage to the lungs. As shown in Fig. S22, computed Tomography (CT) images and the ratio of M2 macrophages in the lungs indicated inflammation occurred after X-ray irradiation, and the treatment with Se@*CM* and *CM* could relieve the inflammation.

Furthermore, these mice were euthanasia and the main organ, whole blood, and serum were collected for further study. Mn-SOD (manganese-superoxide dismutase) is an important antioxidative enzyme that primarily regulates the metabolism of ROS within mitochondria. X-ray irradiation could induce ROS generation and decrease the level of Mn-SOD in serum (Fig. 4G), the treatment of Se@*CM* and *CM* both could significantly inhibit X-ray induced decrease of Mn-SOD, which indicates that *CM* could protect the mitochondria against X-ray irradiation. Troponin (Tn) is a regulatory protein responsible for muscle contraction and relaxation in myocardial tissue. Cardiac troponin (cTn) is a cardiomyocyte-specific antigen, and elevated serum cTn reflects cardiomyocyte damage with high specificity and sensitivity [40]. The serum cTn level was significantly elevated following X-ray irradiation (Fig. 4H), indicating myocardial damage. However, both Se@*CM* and *CM* treatment significantly reduced the level of cTn in serum, indicating the good protection effects of Se@*CM* and *CM* against X-ray irradiation induced damage.

Immune cells play a vital role in the body's fight against inflammation and other diseases, such as T cells and macrophages. Therefore, different immune cells were analyzed by flow cytometry. M2 macrophages are important in anti-inflammatory processes. As shown in Fig. S23, bone marrow-derived macrophages (BMDM) were polarized towards M2 macrophages after being treated with Se@*CM*. The ratios of M2 macrophages in splenocytes and peritoneal macrophages of mice were analyzed by flow cytometry. As shown in Fig. 4I&J, the proportions of M2 macrophages significantly decreased after X-ray irradiation. Interestingly, they were significantly increased after treatment with Se@*CM*, LSe@*CM* and *CM*, with the Se@*CM* treatment group showing the most notable increase. T cells, the main type of lymphocytes, have several biological functions such as killing target cells, responding to antigens and mitogens, and fighting against diseases and tumors. Thus, the proportion of $CD8^+$ T cells and $CD4^+$ T cells in splenocytes were analyzed. As shown in Fig. 4K, the proportion of $CD8^+$ T cells decreased from 7.86 ± 1.19% to 6.58 ± 0.95% after X-ray irradiation. However, it was significantly increased after treatment with Se@*CM*, LSe@*CM*, *CM* and AMI. The Se@*CM* treatment group showed the highest gain in the proportion of $CD8^+$ T cells, with the proportion raised up to 14.04 ± 1.74%. After exposure to X-ray irradiation, the proportion of $CD4^+$ T cells decreased similarly to that of $CD8^+$ T cells. However, the administration of Se@*CM*, LSe@*CM*, *CM* and AMI could reverse the decrease in the proportion of $CD4^+$ T cells. (Fig. 4L). Taken together, these results indicate that Se@*CM* effectively inhibits X-ray-induced cardiomyocyte damage and enhances the anti-inflammatory ability of mice.

To explore the protective effect of Se@*CM* on cardiac function against X-ray irradiation for a relatively long time, three mice from every group were randomly selected for echocardiography after 35 days of the last irradiation (Fig. 5A). The M-mode echocardiograms and mitral flow by PW Doppler Mode of different treatment groups were detected (Fig. 5B&C). Compared to healthy mice, no significant differences in LVEF and LVFS were observed in mice during X-ray exposure (Fig. 5D&E). Additionally, there were no significant differences in the Se@*CM*, LSe@*CM* and *CM* treatment groups between the PBS and X-ray groups. However, the LVPWs and LVPWd of mice in the X-ray irradiation group were still significantly lower than other groups (Fig. 5F&G), which indicated that the heart function disorder induced by X-ray irradiation was still present on day 35th post the last irradiation. Peak E refers to the maximum velocity during the early diastolic period of the mitral valve, while peak A denotes the maximum velocity during the atrial systole. The E/A ratio reveals the effect of atrial contraction on the mitral valve flow. A reduction in the E/A ratio may indicate the degression in ventricular diastolic function. As shown in Fig. 5H, the E/A ratio was decreased after X-ray irradiation, while the Se@*CM/CM* treatment could prevent the decrease, indicating the heart protection of Se@*CM*, LSe@*CM* and *CM*. Besides, treatment of Se@*CM*, LSe@*CM* and *CM* could maintain the Tei index close to the healthy group (Fig. 5I). Furthermore, biochemical indexes of heart function such as aspartate aminotransferase (AST) and lactate dehydrogenase (LDH) was also analyzed. As shown in Fig. 5J&K, the serum levels of AST and LDH significantly increased after X-ray irradiation; however, treatment with Se@*CM*, LSe@*CM* and *CM* effectively attenuated these elevations. The level of Creatine phosphokinase isoenzyme (CK-MB) was found to have slightly decreased after X-ray irradiation (Fig. 6A), and the treatment of Se@*CM*, LSe@*CM* and *CM* could inhibit the decrease of CK-MB. However, the level of cTn tended to normal levels (Fig. 6B). The administration of Se@*CM*, LSe@*CM* and *CM* effectively preserved the level of

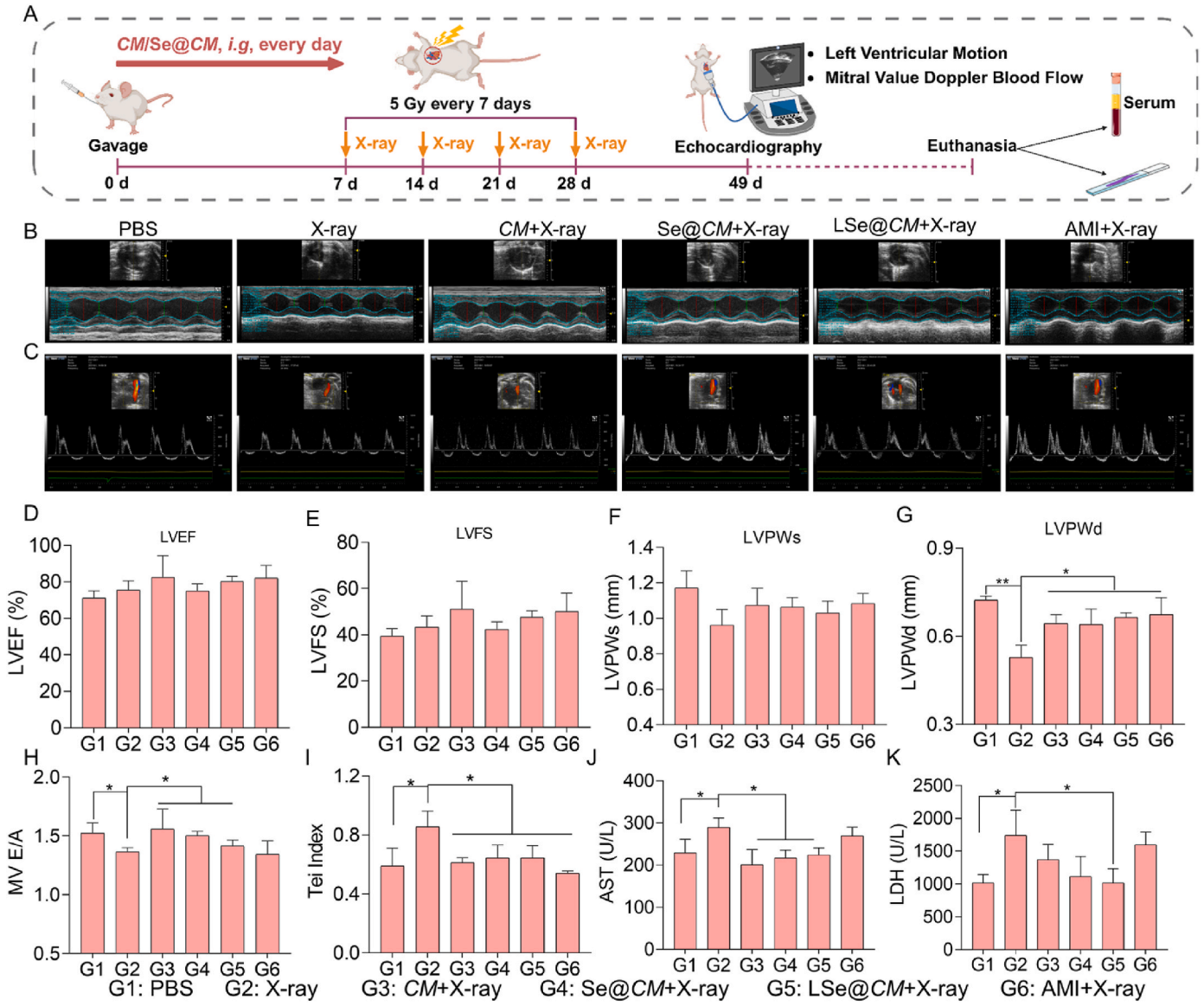

Fig. 5. Long-time protection effect of Se@*CM* on cardiac function against X-ray irradiation-induced damage. (A) A schematic diagram depicting the long-term treatment of mice with Se@*CM* and X-ray irradiation. (B) Echocardiography detection process and representative M-mode echocardiograms for various treatments at day 35 post the last irradiation. (C) Representative echocardiography images of mitral flow by PW Doppler Mode of various treatments after 35 days post the last irradiation. (D) The LVEF, (E) LVFS, (F) LVPWs, (G) LVPWd, (H) mitral velocity E/A ratio (MV E/A), (I) myocardial performance index (MPI, Tei index). (J) Biochemical index of heart function of aspartate aminotransferase (AST), (K) Lactate dehydrogenase (LDH) of different treatments after 35 days post the last irradiation. Each value represents as mean ± SD, n = 3, $^*P < 0.05$.

Mn-SOD and eliminated X-ray-induced lipid peroxidation (Fig. 6C&D). This demonstrates the protective effects of Se@*CM*, LSe@*CM* and *CM* on the heart, shielding it from oxidative damage caused by X-ray exposure.

The biological effects of Se on human and animal health are largely mediated by selenium-containing proteins, which mainly function as oxidoreductase [41]. SEPP and SEPP1 are major selenoproteins that possess antioxidant and Se transportation properties. Upon exposure to X-ray radiation, the expression and secretion of SEPP and SEPP1 in normal cells may be disrupted. As a result, the levels of these proteins increase in response to the buildup of ROS within the cells [42]. As shown in Fig. 6E&F, the levels of SEPP and SEPP1 in serum were significantly increased after X-ray irradiation, however, the treatment of Se@*CM* could significantly inhibit the up-regulation. While the treatment of *CM* and AMI could not change the levels of SEPP and SEPP1. The glutathione peroxidases (GPX) are a major redox system that maintains the reduced state of protein thiols by eliminating intracellular hydrogen and lipid peroxides [43]. As reported, GPX1 plays a crucial role in safeguarding the myocardium against oxidative stress, and its deficiency could lead to cardiomyopathy [44]. In our study, the serum level of GPX1 significantly decreased after X-ray irradiation. However, treatment with Se@*CM* or *CM* could significantly inhibit the decrease of GPX1 (Fig. 6G), which indicated that Se@*CM* or *CM* could alleviate the ROS induced by X-ray irradiation. Selenophosphate Synthetase 2 (SEPHS2), a Se donor compound, is thought to synthesize selenophosphate and is essential for selenoprotein biosynthesis in mammals. The level of SEPHS2 in serum was also inhibited by X-ray irradiation, and treatment with Se@*CM* could enhance the level of SEPHS2 (Fig. 6H). These results indicate that Se@*CM* could enhance the protection effect by regulating the levels of selenoprotein. Except that, the pro-inflammatory cytokines in the serum were analyzed. As illustrated in Fig. 6I&J, the levels of IL-6 and TNF-α in serum were significantly enhanced after X-ray irradiation. However, the treatment with Se@*CM*, *CM* and AMI could inhibit the increase of IL-6 and TNF-α, with the best inhibitory effect of Se@*CM*.

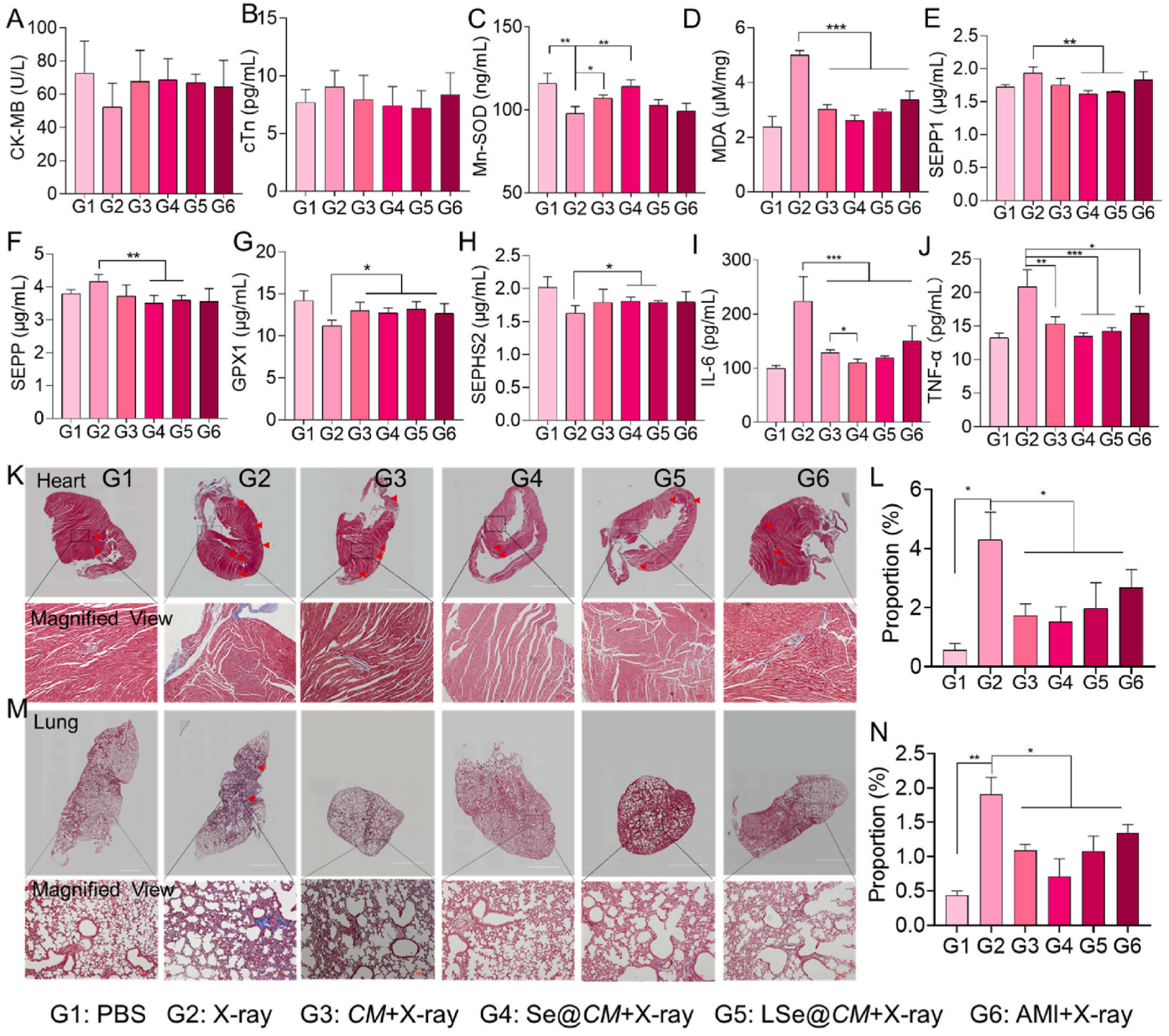

Fig. 6. Hematological and histochemical analysis of Se@*CM* on mice after X-ray irradiation for 35 days. (A) Biochemical index of heart function of Creatine phosphokinase isoenzyme (CK-MB) and (B) cTn. (C) Expression of Mn-SOD and MDA (D). (E) Changes of selenoenzyme in serum of SEPP1, (F) SEPP, (G) GPX1 and (H) SEPHS2. (I) Levels of IL-6 in serum. (J) Levels of TNF-α in serum. (K) Represented images of the heart in different treatment groups by Masson staining and the quantitative analysis of fibrosis area (L). (M) Represented images of lungs in different treatment groups by Masson staining and the quantitative analysis of fibrosis area (N). Each value represents as means ± SD, n = 3, $^{*}P < 0.05$, $^{**}P < 0.01$, $^{***}P < 0.001$.

Masson's trichrome staining assay was then carried out to evaluate the protection efficacy of Se@*CM* on the cardiac structures. As shown in Fig. 6K&L, the fibrosis zone (blue) was significantly enlarged in heart tissue after X-ray irradiation (4.29 ± 0.95%), compared with the PBS group (0.56 ± 0.23%), while the fibrosis zone was significantly decreased in Se@*CM* treatment group (1.52 ± 0.51% for Se@*CM* + X-ray group and 1.97 ± 0.87% for LSe@*CM* + X-ray group, respectively). Meanwhile, the fibrosis zone in *CM* and AMI treatment groups was 1.73 ± 0.39% and 2.68 ± 0.62%, respectively. Moreover, the fibrosis zone in lung tissue was also analyzed and the results as shown in Fig. 6M&N, X-ray irradiation could induce obvious fibrosis in the lungs, and treatment with Se@*CM* could significantly decrease the fibrosis, with a better protective effect than *CM* and AMI treatment. DNA damage could induce activation of phosphorylated ATM (*p*-ATM), the expression of *p*-ATM was examined in heart tissue after X ray exposure. As shown in Fig. S24, the expression level of *p*-ATM was significantly increased after X-ray irradiation. However, *CM*, Se@*CM* and AMI treatment restrained the inducing effects of X-ray. Among them, Se@*CM* showed the best inhibition effect against X-ray as indicated by the decreased expression of *p*-ATM, which suggested the best protection effect of Se@*CM* against X-ray-induced DNA damage. Besides, we detected the expression levels of GPX3 and GPX4, two important antioxidant enzymes in heart tissue. As shown in Fig. S25, X-ray irradiation could suppress the expression of GPX3 and GPX4 in heart tissue, and the treatment of AMI and *CM* could reverse the suppression effects to some extent. However, the expression levels of GPX3 and GPX4 were significant increased after the treatment with Se@*CM*, which indicated that Se@*CM* may exert its role in scavenging free radicals and protecting the myocardium by transforming into selenium-containing proteins with antioxidant functions.

The Se content in major organs was examined using ICP-MS. As

shown in Fig. S26, the oral administration of Se@*CM* could significantly increase the Se content in all major organs, especially in the heart and lungs. The increased content of Se could alleviate ROS induced by X-ray irradiation, thus achieving stronger protection effects. Besides, we examined the routine blood tests to confirm the protective effect of Se@*CM*. Compared with the PBS group, X-ray irradiation markedly decreased the content of white blood cells (WBC), lymphocytes, red blood cells (RBC), and hemoglobin (Hb) (Fig. S27), which indicated that X-ray irradiation had toxic side effects on mice. After Se@*CM* intervention, the content of WBCs, lymphocytes, RBCs and Hb was maintained at a normal level compared with the PBS group. In addition, there was obvious infiltration of the inflammatory cells in heart and lung tissues by H&E staining (Fig. S28), and the treatment of Se@*CM* could significantly reduce the infiltration. Besides, the treatment of Se@*CM* had no obvious toxicity on other major organs, like the liver, kidneys and intestines (Fig. S28). These results demonstrated that Se@*CM* could attenuate the cardiac fibrosis induced by X-ray irradiation, performing long-term protection and recovery effects for the heart from irradiation damage.

3. Discussion

In this study, we used the natural *CM* as a bioactive carrier to efficiently load and deliver Se to achieve enhanced protective effect against X-ray radiation-induced heart damage. The mechanism by which Se@*CM* reverses RIHD involves several key processes: Firstly, RIHD is associated with an increase in ROS production and oxidative stress. Se@*CM* possesses potent antioxidant properties (Fig. 3C–F), promoting the scavenging of ROS and preventing oxidative damage to cardiac tissues. This antioxidant activity helps restore the redox balance in the heart (Fig. S12, Fig. S13), reducing the detrimental effects of radiation. Secondly, radiation exposure leads to an inflammatory response in the heart, contributing to tissue damage. It has been demonstrated that Se@*CM* has anti-inflammatory properties by enhancing the ratio of M2 macrophages (Fig. S23, Fig. 4I and G). By attenuating inflammation, Se@*CM* mitigates the harmful effects of RIHD. Additionally, radiation can induce DNA damage in cardiac cells, leading to genomic instability and dysfunction. Se@*CM* was shown to inhibit DNA damage by inhibiting the level of *p*-ATM, *p*-ATR, and the related protein of DNA damage (Fig. 3G). In summary, Se@*CM* reversed RIHD through the antioxidative, anti-inflammatory, inhibition of DNA damage, these mechanisms help mitigate the detrimental effect of radiation on the heart, promoting tissue repair and the restoration of cardiac function.

In the past few years, we have committed to searching for effective strategies for reversing RIHD, and we have established the radiation-induced myocardial injury model [45]. In the present study, we carried out the experiment as the same procedure as in our previous work. At this radiation dose, the mice showed significant myocardial damage and an ulcer in the tail. Besides, the radiation dose and time intervals for radiotherapy in clinical are individually designed based on the type, size, and location of the tumor. The radiotherapy dose is typically administered in fractionated doses, meaning the total is divided into multiple treatment sessions [46]. Each fractionated dose ranges from 1 to 5 Gy, administered once or once weekly. To simulate the clinical radiotherapy regimen, a total of 20 Gy and a dose of 5 Gy weekly were chosen in this study.

Besides, as per the recommended dietary nutrient intake for Chinese residents, it is advised that adults consume 60 μg of selenium daily. When determining the equivalent dose for both humans and animals, it has been found that each mouse should be given approximately 12.3 μg of Se. In our previous study, SeNPs showed excellent anti-inflammatory effects for atherosclerosis at doses of 0.03 mg/kg and 0.12 mg/kg *via i.v* injection [20]. Besides, considering the anti-inflammatory effects of *CM*, the doses of 0.5 mg/kg and 0.25 mg/kg of Se@*CM* were chosen in our study.

Nevertheless, our current study also has some limitations. Firstly, as a biological carrier, Se@*CM* cannot be fluorescently or otherwise labeled, making it difficult to track the *in vivo* ADME (absorption, distribution, metabolism and excretion) process in real-time. Secondly, although *CM* is a medicinal and edible plant, and the dose used in our experiment is low, further in-depth research is still needed on the pharmacology and toxicology of the drug. Finally, due to the good anti-inflammatory and antioxidant properties of both Se and *CM*, it is important to further characterize their contribution to the overall biological action.

4. Conclusion

Developing novel oral delivery vectors with superior biological regulatory properties, including antioxidative, and anti-inflammatory effects, as well as regulation of immunities, has been identified as a promising strategy for constructing an orally delivered system. Especially, funguses are supposed to be ideal microcarriers due to their rich nutrient content, which can enhance the effectiveness of post-radiotherapy care for patients. In this study, selenium nanoparticles were used as the source of selenium to develop a new system of Se@*CM*. It was found that Se@*CM* exhibited an enhanced protective effect on the heart against X-ray induced damage. Se@*CM* could inhibit X-ray induced G2/M phase arrest of cell cycle and help recover cell proliferation. Additionally, Se@*CM* could reduce X-ray-induced ROS overproduction due to its excellent free radical scavenging ability, and thus prevent DNA damage. Furthermore, Se@*CM* showed a good protective effect on the heart against high doses of X-ray irradiation, as evidenced by the improved cardiac function and less fibrosis zone. Se@*CM* also enhanced the immunity of mice by increasing the ratio of $CD8^+$ T cells, $CD4^+$ T cells and M2 macrophages. The antioxidant capacity of Se@*CM* was significantly enhanced by balancing the selenoproteins. Taken together, this research provides a valuable approach to oral selenium microcarriers based on the fungus for radioprotection and immunohomeostasis shaping against radiation-induced heart disease.

Experiment section

Materials. Lentinan-modified Selenium nanoparticles (LET-SeNPs), Se@*CM* and *CM* were obtained from Guangdong Jinan Established Selenium Source Nano Technology Research Institute Co., Ltd. MTT, DCFH-DA, ABTS (2,2′-azinobis-3-ethylbenzothiazolin-6-sulfonica acid), DPPH (1,1-Diphenyl-2-picrylhydrazyl radical 2,2-Diphenyl-1-(2,4,6-trinitrophenyl) hydroxy), Calcein-AM, PI (propidium iodide), BCA (bicinchoninic acid) assay kits were purchased from Sigma-Aldrich (St. Louis, MO, USA). JC-1 was purchased from MedChemExpress (New Jersey, USA). FBS and DMEM medium were purchased from GIBCO. Mn-SOD and cTn Elisa kits were obtained from Beyotime Biotechnology (Shanghai, China). SEPP1, SEPP, GPX1 and SEPHS2 Elisa kits were obtained from ELISA Genie (London, The United Kingdom). Antibody *p*-ATR (#2853), *p*-CHK1 (#2348), p-H_2A.X (#2577), IRE1-α (#3294), CHOP (#2857), PDI (#3501) and GPX4 (52455) were purchased from Cell Signing Technology (CST). Antibody *p*-ATM (ab315019), SelT (ab176192), SelO (ab172957), GPX2 (ab137431) and GPX3 (ab256470) were purchased from Abcam. Antibody *p*-BRCA1 (PA3148) was purchased from Abmart. Antibody SelS (FNab07705) was purchased from FineTest. Antibody FITC-CD3 (#100204), PE-CD8 (#140408), APC-CD206 (141708), PE-F4/80 (#111704) and FITC-CD11b (#101206) were purchased from BioLegend.

Characterization of Se@*CM*. Se@C*M* were cultured as *CM* except that 60 μg/g of SeNPs was added into the medium of *cordyceps militaris*. The Se contents in Se@*CM* and *CM* were analyzed by Atomic Fluorescence Spectrometer (AFS). The content of cordycepin, cordycepic acid and essential amino acid was analyzed by HPLC, respectively. The chemical composition of Se@*CM* and *CM* was confirmed by UV–vis (Cary 5000 spectrophotometer, Palo Alto).

Cell viability analysis. Rat cardiomyocyte cell line H9C2 was

obtained from ATCC and cultured in DMEM medium supplemented with 10% of FBS and 1% antibiotics (100 U/mL of penicillin and 100 μg/mL of streptomycin) at 37 °C with 5% CO_2 atmosphere. To test the toxicity of Se@*CM* and *CM*, H9C2 cells were seeded in 96-well plates (3×10^3 cells/well). After incubation for one night, the cells were treated with different concentrations of Se@*CM* and *CM* for 72 h. Cell viabilities were examined by MTT assay as reported [47]. To evaluate the protective effect of Se@*CM* and *CM*, H9C2 cells were seeded in 96-well plates (3×10^3 cells/well) overnight and then pre-incubated with different concentrations of Se@*CM* and *CM*. After 24 h, the plates were exposed to X-rays (4, 8 and 16 Gy), respectively. The cell viabilities were examined by MTT assay after 72 h. Besides, the ATP assay was carried out to detect the changes in ATP induced by X-ray irradiation by the ATP assay kit. In addition, the cells were stained with a Calcein-AM/PI double stain kit at different time points and observed by a fluorescence microscope.

Clonogenic assays. The clonogenic assay was performed as previously described [48]. Briefly, H9C2 cells were seeded in 6-well plates with a density of 2×10^3 cells/well and allowed to incubate for 24 h, then the cells were treated with 5 μg/mL of Se@*CM*, *CM* and AMI (2 μM) and incubated for 24 h. Next, the plates were treated with X-rays (0, 4, 8, 16 Gy) and then incubated for 14 days, respectively. Cells were fixed with methanol (30 min), stained with 0.5% of crystal violet solution (30 min), washed with running water, dried and photographed. The surviving fraction was then calculated.

Cell cycle distribution evaluation. The cell cycle distribution assay was conducted by flow cytometry as previously described [49]. Briefly, H9C2 cells were treated with 5 μg/mL of Se@*CM*, *CM* or AMI (2 μM) for 24 h, followed by treatment with/without X-ray (16 Gy). After 72 h, the cells were collected and fixed with 70% cold ethanol for 12 h. After rinsed with PBS twice, the cells were stained with 300 μL of PI in the dark for 30 min. Finally, the cells were analyzed by flow cytometry (Beckman Coulter).

DPPH·and ABTS·free radical scavenging capacity. The free radical scavenging capacity of Se@*CM* to DPPH· and ABTS· was examined by spectrophotometer as previously reported, respectively [50,51]. Briefly, PBS, 10 μg/mL of Se@*CM*, *CM* and 0.2 mM of DPPH solution or ABTS working solution was mixed by 1:1 (v/v), and then the absorbance at 515 nm (DPPH) and 734 nm (ABTS) was recorded within 60 min (Spectra Max M5), respectively.

ROS scavenging activity. The ROS scavenging activity of Se@*CM* and *CM* on H9C2 cells against X-ray irradiation was detected using the DCFH-DA fluorescence probe as previously reported [52,53]. Briefly, H9C2 cells were pre-treated with Se@*CM*, *CM* (5 μg/mL) and AMI (2 μM) for 24 h, then exposed to X-ray (16 Gy). After that, the cells were incubated with DCFH-DA for 30 min at 37 °C, and then a microplate reader (Cytation 5, Bio Tek, USA) was used to measure the levels of intracellular ROS. Simultaneously, fluorescence images were captured at a determined time point by a fluorescence microscope. Besides, after H9C2 cells were exposed to X-ray for 72 h, intracellular ROS was also detected by flow cytometry.

Measurement of mitochondrial potential and morphography. The changes in mitochondrial potential of H9C2 cells after the treatment of Se@*CM* and *CM* were examined by a JC-1 fluorescence probe [54,55]. H9C2 cells were pre-treated with 5 μg/mL of Se@*CM* and *CM* and 2 μM of AMI for 24 h, then exposed to X-ray (16 Gy). After that, cells were collected and incubated with JC-1 (3 μg/mL) for 3omin. After rinsed with PBS, the cells were analyzed using flow cytometry. Simultaneously, fluorescence images were captured by a fluorescence microscope.

Detection of GSH/GSSG. Effects of Se@*CM* on the change of GSH/GSSG were assessed by the GSH/GSSG Ratio Fluorimetric Detection Assay Kit. Briefly, H9C2 cells were pre-treated with Se@*CM*, *CM* (5 μg/mL) and AMI (2 μM) for 24 h, then exposed to X-ray (16 Gy). After that, the cells were collected and detected by following the instructions.

Western blotting analysis. To determine the effects of Se@*CM* and *CM* on protein expression, Western blotting was carried out as previously reported [45,56]. Briefly, H9C2 cells were pretreated with Se@*CM*, *CM* and AMI, then exposed to X-ray. Total protein was extracted using RIPA lysis buffer, quantified using a BCA kit, and 40 μg of protein was loaded onto 12% SDS-PAGE gel for electrophoresis. Afterward, specific antibodies were employed for incubation, followed by the incubation of a secondary antibody. Protein bands were detected using the Tanon 5200 chemiluminescence imaging system, with β-actin serving as an internal control.

Animal experiment. All animal procedures in this study were performed according to the National Institute of Animal Use and Care Committee of Jinan University. BALB/C mice (GemPharmatech, Guangzhou, China) used in this study were about 18–22 g of body weight. For pharmacokinetic and biodistribution studies of Se@*CM*, mice were administrated with Se@*CM* by gavage at the dose of 2 mg/kg Se. At the designated time points, mice were euthanized and serum and major organs were collected for detecting the Se content by using AFS. The animals were divided randomly into 6 groups (n = 10) as follows: PBS, X-ray, *CM* (0.5 mg/kg, every other day, i.g.) with X-ray, Se@*CM* (0.5 mg/kg, every other day, i.g.) with X-ray, LSe@*CM* (0.25 mg/kg, every other day, i.g.) with X-ray, AMI (5 mg/kg, 0.5 h before X-ray, i.p.) with X-ray. The irradiation regimen was in Fig. 5A. On the 7th day after the last irradiation, three mice were randomly selected and the cardiac functions were detected under the Doppler ultrasonic equipment (VISUALISONICS, Vevo 2100 Imaging System, Canada) with an MS-550D probe. The parasternal long-axis view and the motion of the LV wall along with the sampling line were recorded and analyzed in M-mode imaging. The images and many cardiac indices such as fractional shortening (FS), ejection fraction (EF), cardiac output (CO), posterior wall systolic thickness (PWs), posterior wall end-diastolic thickness (PWd), anterior wall end-diastole thickness (AWs), anterior wall end-diastolic thickness (AWd) and so on were recorded. After that, the three mice in every group were euthanized, and the serum was collected and analyzed. The M2 macrophages ($CD11b^+CD206^+$) in the spleen were also analyzed by flow cytometry. The immune cells ($CD3^+CD8^+$ T cell, $CD3^+CD4^+$ T cell) in splenocytes were also examined.

Furthermore, mice were kept feeding and monitored for 2 weeks. In the end experiment, 3 mice in every group were randomly selected for cardiac function analysis by using Doppler ultrasonic equipment. The parasternal long-axis view and mitral valve were recorded and analyzed in M-mode imaging and B-mode. The images and many cardiac indices were also recorded. After that, all mice were euthanized and the serum and main organs (heart, lung, liver, kidney, spleen and intestines) were collected for further study.

Statistical analysis. Experiments were carried out at least three times. Data expressed as the mean ± SD. The level of statistical significance between different groups is carried out by using One-way ANOVA in GraphPad Prim 8.0, (GraphPad Software, San Diego, USA), $^*P < 0.05$, $^{**}P < 0.01$, $^{***}P < 0.001$, and characters of a - g are statistically different at the $P < 0.05$ level.

Ethics

All animal procedures in this study were performed according to the National Institute of Animal Use and Care Committee of Jinan University. The Animal Ethics Number is IACUC-20220408-02.

CRediT authorship contribution statement

Chang Liu: Writing – original draft, Funding acquisition, Formal analysis, Data curation. **Weiyi Wang:** Methodology, Formal analysis, Data curation. **Haoqiang Lai:** Funding acquisition, Data curation. **Yikang Chen:** Supervision, Data curation. **Lvyi Li:** Data curation. **Haiwei Li:** Supervision, Data curation. **Meixiao Zhan:** Methodology. **Tianfeng Chen:** Writing – review & editing, Supervision, Project administration, Funding acquisition. **Wenqiang Cao:** Supervision, Methodology. **Xiaoling Li:** Writing – review & editing, Supervision.

Declaration of competing interest

The authors declare that they have no known competing financial interests or personal relationships that could have appeared to influence the work reported in this paper.

Acknowledgments

This work was supported by the National Science Fund for Distinguished Young Scholars (82225025), National Natural Science Foundation of China (21877049, 32171296, 32101044), Guangdong Natural Science Foundation (2020B1515120043), K. C. Wong Education Foundation and China Postdoctoral Science Foundation (2022M711341).

Appendix A. Supplementary data

Supplementary data to this article can be found online at https://doi.org/10.1016/j.bioactmat.2024.03.034.

References

[1] D.E. Citrin, Recent developments in radiotherapy, N. Engl. J. Med. 377 (2017) 1065–1075, https://doi.org/10.1056/NEJMra1608986.
[2] J.D. Groarke, P.L. Nguyen, A. Nohria, R. Ferrari, S. Cheng, J. Moslehi, Cardiovascular complications of radiation therapy for thoracic malignancies: the role for non-invasive imaging for detection of cardiovascular disease, Eur. Heart J. 35 (2014) 612–623, https://doi.org/10.1093/eurheartj/eht114.
[3] J. Xie, M. Zhao, C. Wang, Y. Yong, Z. Gu, Y. Zhao, Rational design of nanomaterials for various radiation-induced diseases prevention, Adv. Healthcare Mater. (2021) 2001615.
[4] H. Wang, J. Wei, Q. Zheng, L. Meng, Y. Xin, X. Yin, X. Jiang, Radiation-induced heart disease: a review of classification, mechanism and prevention, Int. J. Biol. Sci. 15 (2019) 2128–2138, https://doi.org/10.7150/ijbs.35460.
[5] S. Das, C.J. Neal, J. Ortiz, S. Seal, Engineered nanoceria cytoprotection in vivo: mitigation of reactive oxygen species and double-stranded dna breakage due to radiation exposure, Nanoscale 10 (2018) 21069–21075, https://doi.org/10.1039/c8nr04640a.
[6] J. Guo, Z. Zhao, Z.F. Shang, Z. Tang, H. Zhu, K. Zhang, Nanodrugs with intrinsic radioprotective exertion: turning the double-edged sword into a single-edged knife, Explorations 3 (2023) 20220119, https://doi.org/10.1002/EXP.20220119.
[7] F. Wei, C.J. Neal, T.S. Sakthivel, S. Seal, T. Kean, M. Razavi, M. Coathup, Cerium oxide nanoparticles protect against irradiation-induced cellular damage while augmenting osteogenesis, Mater. Sci. Eng., C 126 (2021) 112145, https://doi.org/10.1016/j.msec.2021.112145.
[8] F. Wei, C.J. Neal, T.S. Sakthivel, Y. Fu, M. Omer, A. Adhikary, S. Ward, K.M. Ta, S. Moxon, M. Molinari, J. Asiatico, M. Kinzel, S.N. Yarmolenko, C.V. San, N. Orlovskaya, R. Ghosh, S. Seal, M. Coathup, A novel approach for the prevention of ionizing radiation-induced bone loss using a designer multifunctional cerium oxide nanozyme, Bioact. Mater. 21 (2023) 547–565, https://doi.org/10.1016/j.bioactmat.2022.09.011.
[9] C. Wang, J. Xie, X. Dong, L. Mei, M. Zhao, Z. Leng, H. Hu, L. Li, Z. Gu, Y. Zhao, Clinically approved carbon nanoparticles with oral administration for intestinal radioprotection *via* protecting the small intestinal crypt stem cells and maintaining the balance of intestinal flora, Small 16 (2020) e1906915, https://doi.org/10.1002/smll.201906915.
[10] J. Gao, T. Hou, Cardiovascular disease treatment using traditional Chinese medicine:mitochondria as the achilles' heel, Biomed. Pharmacother. 164 (2023) 114999, https://doi.org/10.1016/j.biopha.2023.114999.
[11] M.P. Rayman, Selenium and human health, Lancet (2012) 1256–1268.
[12] F. Yang, J. Huang, H. Liu, W. Lin, X. Li, X. Zhu, T. Chen, Lentinan-functionalized selenium nanosystems with high permeability infiltrate solid tumors by enhancing transcellular transport, Nanoscale 12 (2020) 11453–14494, https://doi.org/10.1039/d0nr02171g.
[13] Y. Huang, Y. Fu, M. Li, D. Jiang, C.J. Kutyreff, J.W. Engle, X. Lan, W. Cai, T. Chen, Chirality-driven transportation and oxidation prevention by chiral selenium nanoparticles, Angew. Chem. 132 (2020) 4436–4444, https://doi.org/10.1002/ange.201910615.
[14] C. Liu, H. Lai, T. Chen, Boosting natural killer cell-based cancer immunotherapy with selenocystine/transforming growth factor-beta inhibitor-encapsulated nanoemulsion, ACS Nano 14 (2020) 11067–11082, https://doi.org/10.1021/acsnano.9b10103.
[15] H. Lai, D. Zeng, C. Liu, Q. Zhang, X. Wang, T. Chen, Selenium-containing ruthenium complex synergizes with natural killer cells to enhance immunotherapy against prostate cancer *via* activating TRAIL/FasL signaling, Biomaterials 219 (2019) 119377, https://doi.org/10.1016/j.biomaterials.2019.119377.
[16] T. Liu, L. Xu, L. He, J. Zhao, Z. Zhang, Q. Chen, T. Chen, Selenium nanoparticles regulates selenoprotein to boost cytokine-induced killer cells-based cancer immunotherapy, Nano Today 35 (2020) 100975, https://doi.org/10.1016/j.nantod.2020.100975.
[17] Y. Hu, T. Liu, J. Li, F. Mai, J. Li, Y. Chen, Y. Jing, X. Dong, L. Lin, J. He, Y. Xu, C. Shan, J. Hao, Z. Yin, T. Chen, Y. Wu, Selenium nanoparticles as new strategy to potentiate γδT cell anti-tumor cytotoxicity through upregulation of tubulin-α acetylation, Biomaterials 222 (2019) 119397, https://doi.org/10.1016/j.biomaterials.2019.119397.
[18] Z. Song, W. Luo, H. Zheng, Y. Zeng, J. Wang, T. Chen, Translational nanotherapeutics reprograms immune microenvironment in malignant pleural effusion of lung adenocarcinoma, Adv. Healthcare Mater. 10 (2021) 2100149, https://doi.org/10.1002/adhm.202100149.
[19] H. Yang, C. Liu, Y. Wu, M. Yuan, J. Huang, Y. Xia, Q. Ling, P.R. Hoffmann, Z. Huang, T. Chen, Atherosclerotic plaque-targeted nanotherapeutics ameliorates atherogenesis by blocking macrophage-driven inflammation, Nano Today 42 (2022) 101351, https://doi.org/10.1016/j.nantod.2021.101351.
[20] H. Yang, C. Zhu, W. Yuan, X. Wei, C. Liu, J. Huang, M. Yuan, Y. Wu, Q. Ling, P. R. Hoffmann, T. Chen, Z. Huang, Mannose-rich oligosaccharides-functionalized selenium nanoparticles mediates macrophage reprogramming and inflammation resolution in ulcerative colitis, Chem. Eng. J. 435 (2022) 131715, https://doi.org/10.1016/j.cej.2021.131715.
[21] C. Liu, Y. Fu, C. Li, T. Chen, X. Li, Phycocyanin-functionalized selenium nanoparticles reverse palmitic acid-induced pancreatic β cell apoptosis by enhancing cellular uptake and blocking reactive oxygen species (ros)-mediated mitochondria dysfunction, J. Agric. Food Chem. 65 (2017) 4405–4413, https://doi.org/10.1021/acs.jafc.7b00896.
[22] H. Lai, X. Zhang, Z. Song, Z. Yuan, L. He, T. Chen, Facile synthesis of antioxidative nanotherapeutics using a microwave for efficient reversal of cisplatin-induced nephrotoxicity, Chem. Eng. J. 391 (2020) 123563, https://doi.org/10.1016/j.cej.2019.123563.
[23] J.F. Weiss, M.R. Landauer, History and development of radiation-protective agents, Int. J. Radiat. Biol. 85 (2009) 539–573, https://doi.org/10.1080/09553000902985144.
[24] A. Gehrisch, W. Dörr, Effects of systemic or topical administration of sodium selenite on early radiation effects in mouse oral mucosa, Strahlenther. Onkol. 183 (2007) 36–42, https://doi.org/10.1007/s00066-007-1594-4.
[25] X. Hu, G. Yang, S. Chen, S. Luo, J. Zhang, Biomimetic and bioinspired strategies for oral drug delivery, Biomater. Sci.-Uk 8 (2020) 1020–1044, https://doi.org/10.1039/C9BM01378D.
[26] H. Choi, S.H. Jeong, T.Y. Kim, J. Yi, S.K. Hahn, Bioinspired urease-powered micromotor as an active oral drug delivery carrier in stomach, Bioact. Mater. 9 (2022) 54–62, https://doi.org/10.1016/j.bioactmat.2021.08.004.
[27] Y. Xiao, Z. Tang, J. Wang, C. Liu, N. Kong, O.C. Farokhzad, W. Tao, Oral insulin delivery platforms: strategies to address the biological barriers, Angew Chem. Int. Ed. Engl. 59 (2020) 19787–19795, https://doi.org/10.1002/anie.202008879.
[28] D. Zhang, D. Zhong, J. Ouyang, J. He, Y. Qi, W. Chen, X. Zhang, W. Tao, M. Zhou, Microalgae-based oral microcarriers for gut microbiota homeostasis and intestinal protection in cancer radiotherapy, Nat. Commun. 13 (2022) 1413, https://doi.org/10.1038/s41467-022-28744-4.
[29] S.K. Das, M. Masuda, A. Sakurai, M. Sakakibara, Medicinal uses of the mushroom cordyceps militaris: current state and prospects, Fitoterapia 81 (2010) 961–968, https://doi.org/10.1016/j.fitote.2010.07.010.
[30] F.S. Reis, L. Barros, R.C. Calhelha, A. Ciric, L.J. van Griensven, M. Sokovic, I. C. Ferreira, The methanolic extract of cordyceps militaris (l.) Link fruiting body shows antioxidant, antibacterial, antifungal and antihuman tumor cell lines properties, Food Chem. Toxicol. 62 (2013) 91–98, https://doi.org/10.1016/j.fct.2013.08.033.
[31] J. Liu, C. Feng, X. Li, M. Chang, J. Meng, L. Xu, Immunomodulatory and antioxidative activity of cordyceps militaris polysaccharides in mice, Int. J. Biol. Macromol. 86 (2016) 594–598, https://doi.org/10.1016/j.ijbiomac.2016.02.009.
[32] X. Liu, Y. Huang, Y. Chen, Y. Cao, Partial structural characterization, as well as immunomodulatory and anti-aging activities of CP2-C2-S2 polysaccharide from cordyceps militaris, RSC Adv. (2016) 104094.
[33] J. Liu, C. Feng, X. Li, M. Chang, J. Meng, L. Xu, Immunomodulatory and antioxidative activity of cordyceps militaris polysaccharides in mice, Int. J. Biol. Macromol. 86 (2016) 594–598, https://doi.org/10.1016/j.ijbiomac.2016.02.009.
[34] Y. Zheng, S. Li, C. Li, Y. Shao, A. Chen, Polysaccharides from spores of cordyceps cicadae protect against cyclophosphamide-induced immunosuppression and oxidative stress in mice, Foods 11 (2022), https://doi.org/10.3390/foods11040515.
[35] S.E. Park, J. Kim, Y.W. Lee, H.S. Yoo, C.K. Cho, Antitumor activity of water extracts from cordyceps militaris in NCI-H460 cell xenografted nude mice, J Acupunct Meridian Stud 2 (2009) 294–300, https://doi.org/10.1016/S2005-2901(09)60071-6.
[36] Z. Wang, Z. Chen, Z. Jiang, P. Luo, L. Liu, Y. Huang, H. Wang, Y. Wang, L. Long, X. Tan, D. Liu, T. Jin, Y. Wang, Y. Wang, F. Liao, C. Zhang, L. Chen, Y. Gan, Y. Liu, F. Yang, C. Huang, H. Miao, J. Chen, T. Cheng, X. Fu, C. Shi, Cordycepin prevents radiation ulcer by inhibiting cell senescence *via* NRF2 and AMPK in rodents, Nat. Commun. 10 (2019), https://doi.org/10.1038/s41467-019-10386-8.
[37] M. Chen, X. Huang, J. Lai, L. Ma, T. Chen, Substituent-regulated highly X-ray sensitive os(vi) nitrido complex for low-toxicity radiotherapy, Chin. Chem. Lett. 32 (2021) 158–161, https://doi.org/10.1016/j.cclet.2020.11.050.
[38] Y. Duo, Y. Huang, W. Liang, R. Yuan, Y. Li, T. Chen, H. Zhang, Ultraeffective cancer therapy with an antimonene-based X-ray radiosensitizer, Adv. Funct. Mater. 30 (2019) 1906010, https://doi.org/10.1002/adfm.201906010.
[39] M. Chen, W. Cao, J. Wang, F. Cai, L. Zhu, L. Ma, T. Chen, Selenium atom-polarization effect determines TrxR-specific recognition of metallodrugs, J. Am. Chem. Soc. 144 (2022) 20825–20833, https://doi.org/10.1021/jacs.2c08802.

[40] H. Wang, J. Liu, J. Zhao, L. Lin, W. Zhao, P. Tan, W. Tian, B. Zhou, Ca^{2+} metabolic disorder and abnormal expression of cardiac troponin involved in fluoride-induced cardiomyocyte damage, Chemosphere 201 (2018) 564–570, https://doi.org/10.1016/j.chemosphere.2018.03.053.
[41] V.M. Labunskyy, D.L. Hatfield, V.N. Gladyshev, Selenoproteins: molecular pathways and physiological roles, Physiol. Rev. 94 (2014) 739–777, https://doi.org/10.1152/physrev.00039.2013.
[42] J.C. Eckers, A.L. Kalen, W. Xiao, E.H. Sarsour, P.C. Goswami, Selenoprotein p inhibits radiation-induced late reactive oxygen species accumulation and normal cell injury, Int. J. Radiat. Oncol. 87 (2013) 619–625, https://doi.org/10.1016/j.ijrobp.2013.06.2063.
[43] N. Weiss, Y.Y. Zhang, S. Heydrick, C. Bierl, J. Loscalzo, Overexpression of cellular glutathione peroxidase rescues homocyst(e)ine-induced endothelial dysfunction, Proc Natl Acad Sci U S A 98 (2001) 12503–12508, https://doi.org/10.1073/pnas.231428998.
[44] C. Lei, X. Niu, J. Wei, J. Zhu, Y. Zhu, Interaction of glutathione peroxidase-1 and selenium in endemic dilated cardiomyopathy, Clin. Chim. Acta 399 (2009) 102–108, https://doi.org/10.1016/j.cca.2008.09.025.
[45] C. Dai, L. He, B. Ma, T. Chen, Facile nanolization strategy for therapeutic ganoderma lucidum spore oil to achieve enhanced protection against radiation-induced heart disease, Small 15 (2019) e1902642, https://doi.org/10.1002/smll.201902642.
[46] W. Mao, J. Riess, J. Kim, S. Vance, I.J. Chetty, B. Movsas, A. Kretzler, Evaluation of auto-contouring and dose distributions for online adaptive radiation therapy of patients with locally advanced lung cancers, Pract Radiat Oncol 12 (2022) e329–e338, https://doi.org/10.1016/j.prro.2021.12.017.
[47] Y. Duo, Z. Chen, Z. Li, X. Li, Y. Yao, T. Xu, G. Gao, G. Luo, Combination of bacterial-targeted delivery of gold-based aiegen radiosensitizer for fluorescence-image-guided enhanced radio-immunotherapy against advanced cancer, Bioact. Mater. 30 (2023) 200–213, https://doi.org/10.1016/j.bioactmat.2023.05.010.
[48] R. Chai, L. Yu, C. Dong, Y. Yin, S. Wang, Y. Chen, Q. Zhang, Oxygen-evolving photosynthetic cyanobacteria for 2D bismuthene radiosensitizer-enhanced cancer radiotherapy, Bioact. Mater. 17 (2022) 276–288, https://doi.org/10.1016/j.bioactmat.2022.01.014.
[49] Z. Song, T. Liu, H. Lai, X. Meng, L. Yang, J. Su, T. Chen, A universally EDTA-assisted synthesis of polytypic bismuth telluride nanoplates with a size-dependent enhancement of tumor radiosensitivity and metabolism *in vivo*, ACS Nano 16 (2022) 4379–4396, https://doi.org/10.1021/acsnano.1c10663.
[50] L. He, G. Huang, H. Liu, C. Sang, X. Liu, T. Chen, Highly bioactive zeolitic imidazolate framework-8-capped nanotherapeutics for efficient reversal of reperfusion-induced injury in ischemic stroke, Sci. Adv. 6 (2020) y9751, https://doi.org/10.1126/sciadv.aay9751.
[51] L. Feng, L. Wang, Y. Ma, W. Duan, S. Martin-Saldaña, Y. Zhu, X. Zhang, B. Zhu, C. Li, S. Hu, M. Bao, T. Wang, Y. Zhu, F. Yang, Y. Bu, Engineering self-healing adhesive hydrogels with antioxidant properties for intrauterine adhesion prevention, Bioact. Mater. 27 (2023) 82–97, https://doi.org/10.1016/j.bioactmat.2023.03.013.
[52] K. Shen, G. Sun, L. Chan, L. He, X. Li, S. Yang, B. Wang, H. Zhang, J. Huang, M. Chang, Z. Li, T. Chen, Anti-inflammatory nanotherapeutics by targeting matrix metalloproteinases for immunotherapy of spinal cord injury, Small 17 (2021) 2102102, https://doi.org/10.1002/smll.202102102.
[53] J. Li, C. Deng, W. Liang, F. Kang, Y. Bai, B. Ma, C. Wu, S. Dong, Mn-containing bioceramics inhibit osteoclastogenesis and promote osteoporotic bone regeneration *via* scavenging ROS, Bioact. Mater. 6 (2021) 3839–3850, https://doi.org/10.1016/j.bioactmat.2021.03.039.
[54] Z. Yuan, X. Liu, J. Ling, G. Huang, J. Huang, X. Zhu, L. He, T. Chen, *In situ*-transition nanozyme triggered by tumor microenvironment boosts synergistic cancer radio-/chemotherapy through disrupting redox homeostasis, Biomaterials 287 (2022) 121620, https://doi.org/10.1016/j.biomaterials.2022.121620.
[55] W. Huang, S. Shi, H. Lv, Z. Ju, Q. Liu, T. Chen, Tellurium-driven maple leaf-shaped manganese nanotherapeutics reshape tumor microenvironment via chemical transition *in situ* to achieve highly efficient radioimmunotherapy of triple negative breast cancer, Bioact. Mater. 27 (2023) 560–573, https://doi.org/10.1016/j.bioactmat.2023.04.010.
[56] H. Lai, C. Liu, L. Hou, W. Lin, T. Chen, A. Hong, TRPM8-regulated calcium mobilization plays a critical role in synergistic chemosensitization of borneol on doxorubicin, Theranostics 10 (2020) 10154–10170, https://doi.org/10.7150/thno.45861.